SDSS IV MaNGA: Inside-out quenching galaxies with Hα ring-like structures

Jiaxuan Li,[1] Yingjie Peng,[2] Kexin Guo,[2] Song Huang,[3] and Chengpeng Zhang[2]

[1]*Department of Astronomy, School of Physics, Peking University*
5 Yiheyuan Road, Haidian District, Beijing, 100871, China
[2]*Kavli Institute of Astronomy and Astrophysics, Peking University*
5 Yiheyuan Road, Haidian District, Beijing, 100871, China
[3]*Department of Astronomy and Astrophysics, University of California Santa Cruz*
1156 High St., Santa Cruz, CA 95064, USA

ABSTRACT

We investigated galaxies with Hα emission ring-like structures in Mapping Nearby Galaxies at APO (MaNGA) survey, with stellar mass in the range of $10.0 < \log(M/M_\odot) < 11.5$ and redshift $0.02 < z < 0.14$. About 80% of these galaxies are located in the "green valley" and experiencing inside-out quenching process. The Hα ring galaxies also account for 20% – 30% of green valley galaxies. We measure the radii of Hα rings and find that bars are just stuck in the Hα rings. Bar fraction in Hα ring galaxy sample is 20% – 30% higher than that of total galaxies, indicating the tight relation between bars and Hα rings. The majority (90%) of galaxy nuclei in our Hα ring galaxy sample are LINER and retied galaxies (RG) classified using BPT diagrams, and these galaxies are mostly diagnosed as cLIERs when using BPT spacial map. Compared to the total sample, the AGN (Seyfert/LINER) fraction and bulge-to-total ratio are also higher in Hα ring sample for about 10%. Our findings support that the joint effects of bar, bulge and AGN could quench the massive disk galaxies efficiently by the inside-out quenching mode and form the Hα ring-like structure. This may reveal a major quenching mechanism for massive disk galaxies.

Keywords: galaxy: evolution – galaxies: structure – galaxy: nucleus

1. INTRODUCTION

The morphology of galaxy has long been the focus of galaxy researchers. Edwin Hubble classified galaxies into spiral, elliptical or irregular galaxies and came up with the so-called Hubble sequence (Hubble 1926). Later studies show that star formation histories, dynamical evolution of galaxy could engrave imprints on galaxy morphology. Morphology provides us a window to get insights into galaxy formation and evolution. An interesting structure of galaxy is optical ring structure, which mainly appears in disk galaxies. Few & Madore (1986) studied nearby optical ring galaxies and divided them into P-type or O-type. P-type optical ring galaxies often have crisp, knotty structures and displaced nuclei, whereas O-type optical ring galaxies are smooth and their nuclei are at the center. P-type optical ring galaxies are believed to be the results of galaxy interactions and mergers, which has been proved by the state-of-art cosmological simulations (e.g. Elagali et al. 2018). O-type optical ring galaxies are mostly the resonance ring galaxies (Buta 2017), often associated with strong bars and look like "Θ" shapes. Resonance could slowly change the structure of a galaxy, making it as an important factor in the secular evolution of disk galaxies (Kormendy 2013).

In the dynamics of spiral arms and bars in disk galaxies, one of the most significant resonance is Lindblad resonance. The inner and outer ring can be naturally formed due to Lindblad resonance. Gas at small radii gives up some angular momentum and falls towards the center. Gas at the end of the bar is focused into a ring around the bar, seen as the inner ring. Gas at large radii gains angular momentum, moves to larger radii and is guided into an outer ring near outer Lindblad resonance. Besides, the bar can transport the gas towards the center region and build a pseudo-bulge (e.g. Kormendy & Kennicutt 2004, Kruk et al. 2018).

Previous studies on galaxy morphology mainly focus on optical images. Recently, taking the advantage of the prevalent integral field units (IFU) surveys, the morphology of galaxies under emission lines is studied (e.g. Belfiore et al. 2016, 2017; Guo et al. 2019), which could reveal important physical properties of galaxies, including kinematics of gas, stellar age and metallicity gradients, and active galactic nuclei (AGN) activities.

Emission line images are also used to study the quenching process of galaxies. We consider the term *quenching* here to mean the cessation of star formation in any region of a galaxy. Observationally, quenching is the process that causes the change of galaxy color and color gradient, accompanied with the mi-

gration of galaxies from "blue cloud", where the star formation continues, to the "red sequence", where it is assumed that star formation activities are so suppressed as to be negligible. Studies have shown two primary quenching channels: environment-dependent channel, which mainly acts on low mass galaxies and satellite galaxies, and mass-dependent channel, which could be triggered by various internal processes (Peng et al. 2010). Environment-dependent channel is usually related to cosmological strangulation (Peng et al. 2015) and ram pressure stripping (Larson et al. 1980). However, the uncertainties on the mechanisms of mass-dependent quenching still exist, especially on the roles of AGN feedback, bar-induced activities, morphological quenching and other internal processes.

Previous works have found two distinct quenching modes of galaxies, termed as "inside-out" and "outside-in" quenching in the literature (Sánchez-Blázquez et al. 2007; Li et al. 2015). In the "inside-out" scenario, the disk instability of a disk galaxy will induce gas inflow and trigger starburst in the galactic center. Besides of star formation, the inflow gas can also fuel the central supermassive black hole and trigger AGN activities. AGN could blow the gas out of the central region of the galaxy and heat the gas to prevent further star formation. This effect is called "AGN feedback" and is able to suppress the star formation in the central part. In the meantime, the outskirts still have relatively high star formation rate (Dekel & Burkert 2014). Many works have found that massive spiral galaxies have negative color gradients or stellar age gradients, which support this "inside-out" picture (Wang et al. 2011; Pérez et al. 2013; Pan et al. 2015). Observations also show that the evolution of low mass galaxies can be better interpreted in an "outside-in" framework (Gallart et al. 2008; Pan et al. 2015). Low mass galaxies have shallower potential wells, making them less capable to accretion gas and form stars in the outskirts.

Previous observational diagnosis on "inside-out" and "outside-in" quenching modes are mainly based on color and stellar age gradients. With IFU surveys such as CALIFA (Sánchez et al. 2012), SAMI (Croom et al. 2012) and MaNGA (Bundy et al. 2015), quenching modes can be studied more precisely and the effects of internal processes on mass-dependent quenching can be studied from more perspectives with much higher resolution. In the "inside-out" scenario, the central region has ceased star formation, while the outskirts still have star formation. The star-forming ring naturally emerges from this scenario. Since active star-forming region emits strong Hα photons and AGN is also a strong Hα source, we suggest that inside-out quenching disk galaxies should have an Hα ring-like structure, with a bright Hα emission core and an Hα emission deficient area inside this ring.

In this paper, with the help of IFU survey, we select 84 galaxies with Hα star-forming ring, and investigate the effect of both internal and external factors on the "inside-out" quenching of these galaxies. We use public data from MaNGA v2_1_2 in SDSS DR14, combining with Galaxy Zoo, Mendel et al. (2014) galaxy disk-bulge decomposition catalog, MPA-JHU DR7 catalogs (Brinchmann et al. 2004) and environment over-density catalog (Peng et al. 2010). The layout of this paper is as follows. The data and sample selection are described in Section 2. In Section 3, we measure the radii of Hα rings and reveal the strong correlation between Hα ring and the existence of bar. The dependence of Hα rings on bar, AGN and bulge is presented in Section 4. Discussions on our results and related topics is included in Section 5. In this paper we adopt a ΛCDM cosmology with $\Omega_m = 0.27$, $\Omega_\Lambda = 0.73$ and $H_0 = 71$ km^{-1} s^{-1} Mpc^{-1}. We adopt the Salpeter Initial Mass Function (IMF, Salpeter 1955) in spectroscopic analysis and convert the results based on other IMF to the Salpeter one.

2. DATA AND SAMPLE

2.1. *MaNGA Survey*

Mapping Nearby Galaxies at Apache Point Observatory (MaNGA) survey is a part of Sloan Digital Sky Survey-IV (SDSS-IV). The MaNGA instrument suite is mounted on the SDSS 2.5 m telescope at APO (Gunn et al. 2006) and is described in Drory et al. (2015) with more details. Unlike previous SDSS surveys which only obtained spectra of galaxies within a certain aperture size (typically 2-3 arcsec), MaNGA simultaneously uses 17 hexagonal integral field units (IFUs) to obtain spatially resolved spectra for about 10,000 nearby galaxies, which cover 2700 deg^2 area on the sky (Bundy et al. 2015). Each IFU is composed of tightly-packed arrays of optical fibers, the number of fibers is ranged from 19 (12 arcsec diameter) to 127 (32 arcsec diameter) with a 56% filling factor. Twelve additional minibundles (7 fibers each) are used for flux calibration and 92 single fibers are used for sky subtraction. The point spread function (PSF) usually ranges from 2.5 arcsec to 3 arcsec.

These IFUs are split to feed the two BOSS spectrographs. BOSS spectrographs have a wavelength coverage of 3600 - 10300Å and a spectral resolution of $R \sim 2000$ ($R \sim 1600$ at 4000 Å, and $R \sim 2300$ at 8500 Å) (Smee et al. 2013). Each MaNGA plate is exposed until it reaches a fixed target signal to noise ratio (S/N). Roughly three hour dithered exposures are applied to compensate for light loss between fibers and to obtain a uniform circular PSF (Law et al. 2015). Since every pixel of a galaxy has spectral measurement, we refer to the MaNGA pixels in the spatial dimension as *spaxels* for convenience.

The MaNGA sample is selected from the NASA-Sloan Atlas[1] with redshifts mostly from the SDSS Data Re-

---

lease 7 main galaxy sample (Abazajian et al. 2009). The MaNGA sample is constructed aiming at observing 10,000 nearby galaxies, with a flat number density distribution in i-band absolute magnitude M_i (as a proxy for stellar mass). The design of MaNGA sample also maximizing the spatial resolution and S/N while satisfying the above requirements. A more detailed description can be found in Wake et al. (2017). MaNGA target galaxies are divided into 'primary' and 'secondary' sample, following a 3:1 ratio. MaNGA aims to obtain radial coverage out to at least 1.5 R_e (2.5 R_e) for primary sample (secondary sample), respectively. The mean redshift of the total MaNGA sample is $\bar{z} \sim 0.03$, while galaxies in secondary sample are generally at higher redshift ($\bar{z} \sim 0.045$).

2.2. MaNGA Pipe3D Value Added Catalog

As the main source of the data used in this work, MaNGA Pipe3D Value Added Catalog (Pipe3D VAC) is data products and catalogs extracted from the MaNGA datacubes using the Pipe3D pipeline (Sánchez et al. 2018). Pipe3D pipeline characterizes the properties of the stellar populations and ionized gas emission lines in the spatially resolved data of optical IFU surveys, including CALIFA, MaNGA and SAMI (Sánchez et al. 2016).

Pipe3D produces a single FITS file for each galaxy in MaNGA data release v2_1_2. Each file comprises five extensions: The first extension corresponds to the header of the original data cube (including the World Coordinate System WCS), and the remaining four extensions contain data of stellar population properties, star formation histories, emission line fluxes and stellar absorption line indices of each spaxel.

In addition, Pipe3D VAC also provides a catalog containing the overall properties of galaxies in MaNGA data release version v2_1_2. It includes integrated properties (e.g., stellar mass, star-formation rate), and the characteristic values of emission lines (e.g. oxygen abundance at the effective radius), together with other relevant information about the galaxy (e.g. ionization conditions in the center of the galaxy). Detailed description can be found in MaNGA Pipe3D Data Model[2]. Hereinafter we refer to these datacubes as Pipe3D Cubes and refer to this catalog as Pipe3D Catalog.

Pipe3D adopted the miles12 SSP library (Sánchez 2006; Vazdekis et al. 2010; Falcón-Barroso et al. 2011) and the Salpeter IMF (Salpeter 1955). Star formation rate (SFR) of each spaxel is estimated using the Hα flux (Kennicutt 1998) after performing dust attenuation corrections using the Hα/Hβ ratio. SFR of a galaxy in Pipe3D Catalog is calculated by summing

---

[2] https://data.sdss.org/datamodel/files/MANGA_PIPE3D/ MANGADRP_VER/PIPE3D_VER/PLATE/manga.Pipe3D. cube.html

up SFRs spaxel-by-spaxel across MaNGA field of view (FoV) (Sánchez et al. 2016). In this paper, we only consider the SFR within MaNGA FoV. In total, Pipe3D VAC provides the data products for 2755 out of 2810 galaxies included in MaNGA data release v2_1_2, with the remaining have issues with the data processing. After removing the repeated observations, we have 2704 galaxies in the *total sample* of this work. Without special notification, we use Pipe3D-derived physical quantities of galaxies (e.g. star formation rate, stellar mass, equivalent width of emission line, etc) in the following of this paper.

2.3. Hα Ring Galaxy Sample Selection

We construct the Hα ring galaxy sample in which galaxies have Hα ring-like star-forming structures by visually inspecting the tri-color emission-line images generated by ourselves based on Pipe3D Cubes. In the emission-line image (lower panels in Figure 1), red, green and blue color stand for [N II] 6584Å, Hα 6563Å and [O III] 5007Å emission line fluxes in the corresponding spaxels. The criteria for diagnosing an Hα ring in this work are: (1) an Hα ring-like structure appears in the FoV of tri-color emission-line image; (2) the ring-like structure is not required to be closed, but it should not be too shattered at lease; (3) a dark Hα gap between the central region and the ring-like structure can be found in the tri-color emission-line image.

We construct a relatively conservative *Hα ring galaxy sample* which contains 84 galaxies with clear Hα ring-like structures. Figure 1 shows four randomly selected galaxies in Hα ring galaxy sample. The emission-line images are adjusted into the same size as the corresponding optical images in the upper panels. The first two galaxies do not have bars and optical rings, while the other two have bars and prominent optical rings. Optical rings here could be Lindblad inner rings. In addition, we visually check the morphology of galaxies in this Hα ring galaxy sample, 44 galaxies have bars and the others are unbarred. We do not limit the morphology of Hα ring galaxies when selecting them, only very few of them ($\sim$5%, based on visual inspection) are elliptical galaxies.

The distributions of total sample and Hα ring sample are shown on the stellar mass M_* – SFR plane in Figure 2. Galaxies in total sample are drawn in dots, color-coded by SFR. They are distributed mainly in the two sequence: main sequence (MS) and passive sequence (PS). Between the two sequences lies green valley (GV). We define GV to be galaxies between $\log \text{SFR} = \log(M_*/M_\odot) - 10.7$ and $\log \text{SFR} = \log(M_*/M_\odot) - 11.5$ (the two yellow lines in Figure 2). Galaxies in Hα ring sample are shown in pentagrams, color-coded by whether they are barred or unbarred (inspected by eyeballs) and excitation types. Retired galaxies (see Section 4.2) in Hα ring sample are presented by pentagrams with gray centers. It is clear that Hα ring galaxies mainly lie in the Green Valley. Slight change in the definition of

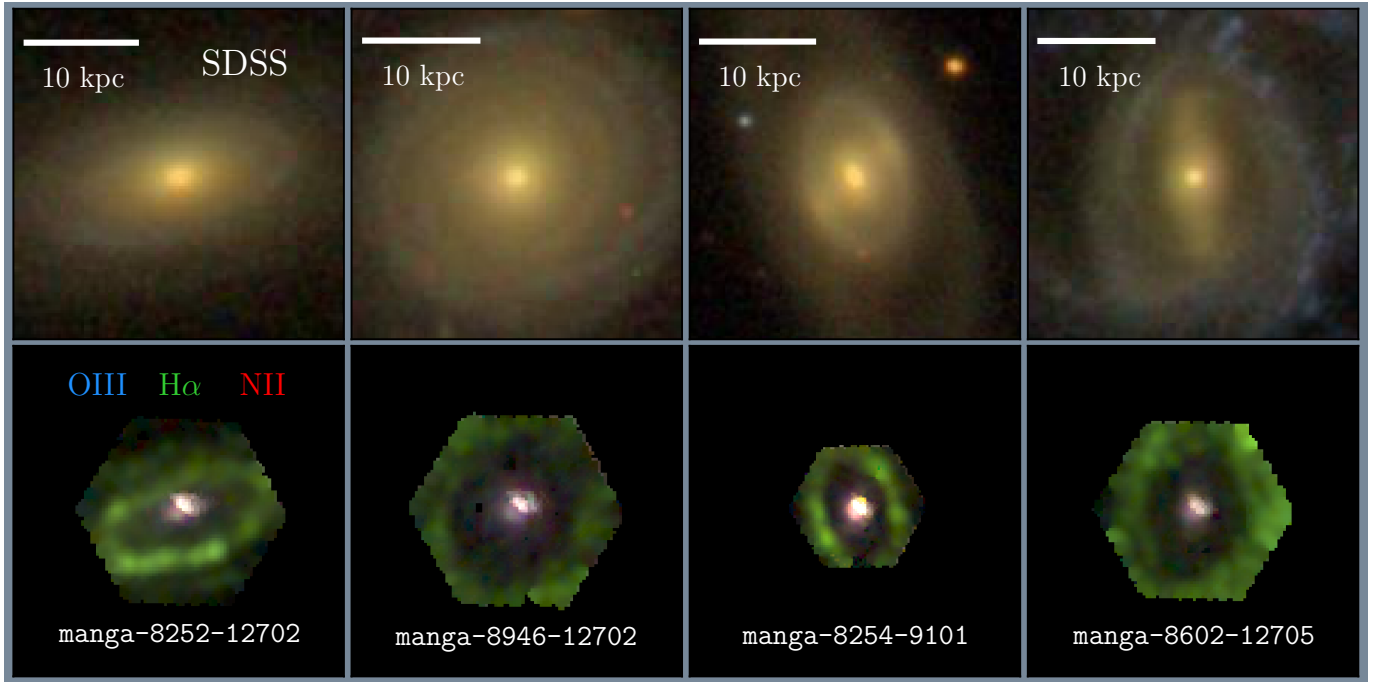**Figure 1.** Four randomly selected galaxies with Hα ring-like star-forming structures in MaNGA Pipe3D v2_1_2 sample. The upper images are optical images from SDSS photometry data. The lower images are corresponding tri-color emission-line images from MaNGA, in which red, green, blue represent for [NII] 6584Å, Hα, [OIII] 5007Å emission line fluxes, respectively. The first two galaxies do not have bars and prominent optical rings, while the other two have bars and O-type optical rings.

GV doesn't change this conclusion. The void of star formation within the Hα ring is consistent with the prediction of an inside-out quenching picture.

Figure 2 also shows redshift and stellar mass distributions in both samples. The redshift of galaxies in Hα ring galaxy sample range from 0.02 to 0.14, with 90.5% redshift less than 0.08. Stellar mass of galaxies in Hα ring galaxy sample ranges from $10^{9.5}M_\odot$ to $10^{11.5}M_\odot$, with only one galaxy's stellar mass less than $10^{10}\ M_\odot$. Most galaxies (85.7%) are massive disk galaxies ($M_* > 10^{10.5}M_\odot$). Hα ring galaxy sample is more concentrated in the high mass region, whereas total sample is distributed rather flat along stellar mass. This bias is probably induced by the Hα sample selection criteria since low mass galaxies are fainter and less capable of showing prominent Hα ring-like structures in the emission-line images. But the inside-out quenching mode is indeed observed in massive disk galaxies rather than in low mass and satellite galaxies (Ref. here). Besides, massive disk galaxies are less prone to be affected by environment, making them good objects to study internal processes in the inside-out quenching.

The population of Hα ring galaxies is not a minority in the Green Valley. We show the moving average of Hα ring galaxies fractions with 1 dex sSFR bin width and 0.1 dex moving step in Figure 3. Since we are prone to select face-on Hα ring galaxies and the distributions of b/a above $b/a > 0.5$ are nearly identical for both sample, we only select galaxies with $b/a > 0.5$ to calculate the

Hα ring galaxy fraction in GV. It turns out that 75 (out of 84) Hα ring galaxies and 67.3% galaxies in total sample satisfy this inclination threshold. Based on the mass distribution, galaxies are divided into three mass bins: $\log M_*/M_\odot = [10.0, 10.5]$, $[10.5, 11.0]$ and $[11.0, 11.5]$, and the Hα ring galaxy fractions in each mass bin are shown by different colors. The moving average lines reveal how Hα ring galaxy fractions change with increasing specific Star Formation Rate (sSFR). The shaded area indicates the Green Valley as defined above. The fractions of Hα ring galaxies show unimodal distributions, with their peaks all locate within the Green Valley. In general, around 20% - 30% massive disk galaxies in GV have Hα ring-like structures. Noticing that the definition of GV could affect this results, we tested several different GV definitions and didn't find conspicuous differences. Nevertheless, this fraction is obviously underestimated since our Hα ring galaxy sample is very conservatively selected. Hence, Hα ring galaxies could account for a large proportion in GV and deserve specific studies on their quenching process.

3. RADII OF Hα RING-LIKE STRUCTURE

Visual inspections of optical images reveal that Hα rings might have correlation with optical rings and bars. Indeed, Kormendy (2013) suggests that optical ring typically contains HI gas and has active star formation. In this section, we measure the radii of Hα rings for barred galaxies in Hα ring galaxy sample to study the correlation between Hα rings and bars. The left panel of Figure
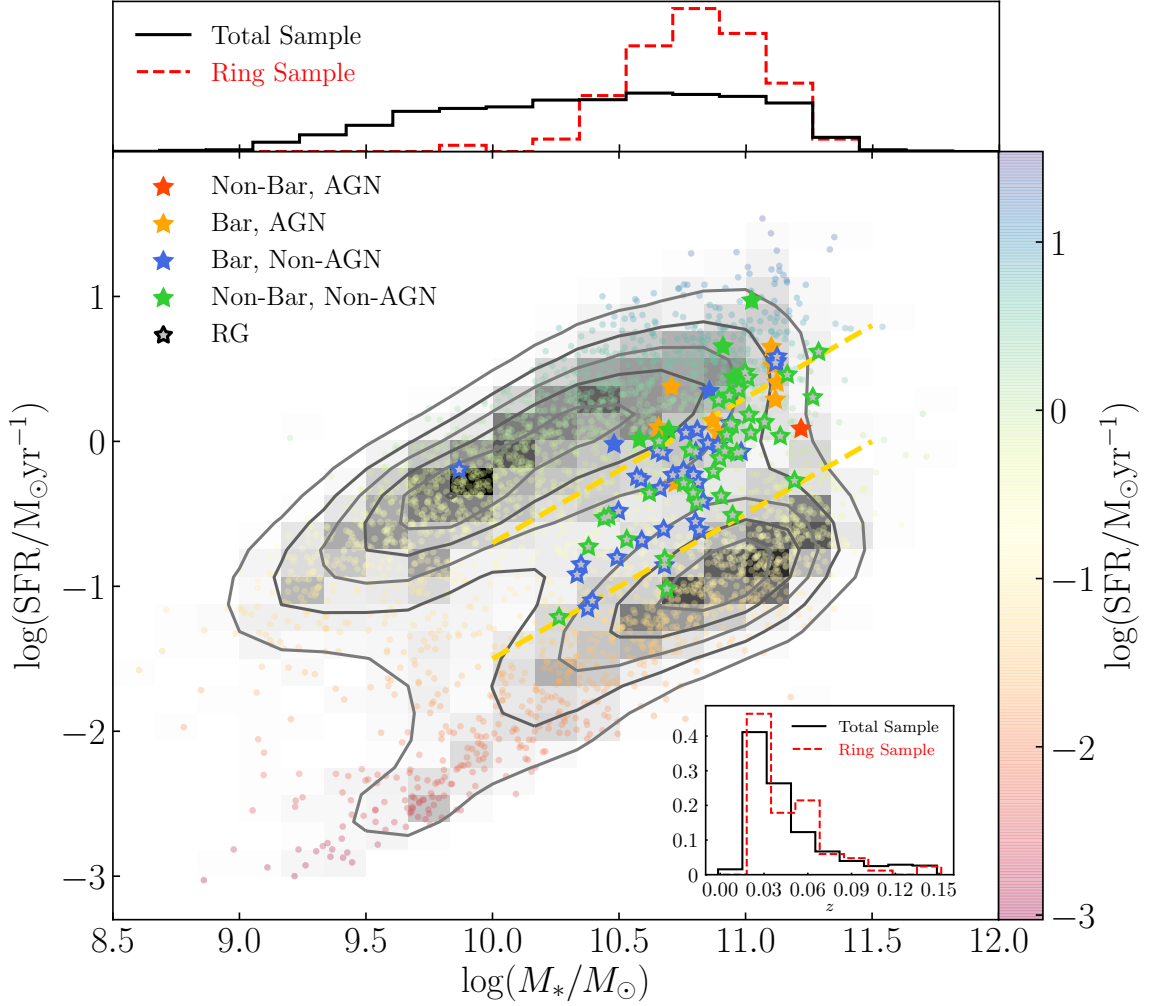
Figure 2. Distribution of galaxies in both total sample and Hα ring galaxy sample on stellar mass M_* – SFR plane. Stellar mass M_* and SFR are both adopted from Pipe3D Catalog. Galaxies in total sample are drawn in small dots, color-coded by $\log \mathrm{SFR}$. Pentagrams are Hα ring galaxies, color-coded by their excitation types and morphology (inspected by eyeballs). The total sample is distributed along main sequence (MS) and passive sequence (PS), and galaxies in Hα ring galaxy sample are mainly distributed in the green valley (GV, marked by two yellow lines). This figure also shows the mass and redshift distributions of both samples.

4 shows the Hα image of galaxy `manga-8450-6101`. We extract Hα fluxes from Pipe3D Cubes, and the shapes (position angle and b/a ratio) of galaxies are extracted from Pipe3D Catalog. By applying polar transformation $(x, y, flux) \rightarrow (r, \theta, flux)$ to the Hα image, we can get the radial distribution profiles of Hα flux for every polar angle in $\theta \in (0, 2\pi)$. We set the starting point of polar transformation to the position angle to avoid the uncertainty caused by extra interpolation in rotating the image. We denote the Hα flux profiles as $f(r, \theta)$, where θ is polar angle starting from the semi-major axis of a galaxy.

Because of the existence of inclination between the galaxy and sky plane, it's necessary to deproject these profiles before stacking them. Under the assumption that a closed Hα ring is intrinsically circular , we stretch the flux profile $f(r, \theta)$ by a factor of $\xi(\theta) =$

$\sqrt{\cos^2 \theta + (\sin \theta/(1 - e)^2}$, where $1 - e = b/a$ is the semi-minor to semi-major ratio of disk galaxies. Thus $\tilde{f}(r, \theta) = f(\xi(\theta)r, \theta)$ is the deprojected profiles. Then these deprojected profiles of each polar angle θ are stacked together to make the final Hα flux profile (see the right panel of Figure 4 as an example). The shaded area around the profile represents 1σ uncertainty, which is calculated from the standard deviation of fluxes at a fixed radial distance before stacking.

The Hα flux profile has one trough outside the central peak and a second peak outside the trough. The trough and second peak correspond to the dark gap and Hα ring in 2-dimensional Hα image distribution (upper-right panel in Figure 4). Using peak detecting tool `PeakUtils`, the positions of both trough and peak can be determined. In Hα ring galaxy sample, 79 galaxies (out of 84) have trough detection, and 71 galaxies (out
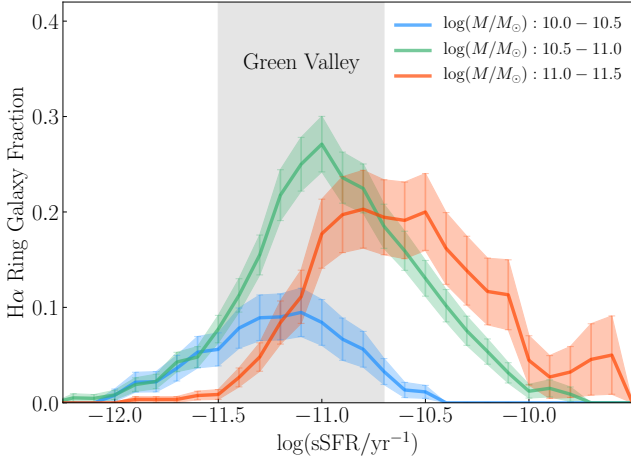
Figure 3. The fractions of Hα ring galaxy in total galaxy sample. We only consider galaxies with $b/a > 0.5$. The shaded area shows Green Valley which is defined above and shows as galaxies between the two yellow lines in Figure 2. Moving average lines shows that Hα ring galaxy fractions achieve peaks in Green Valley. The lower limit of Hα ring galaxy fraction in massive disk galaxies is around 20%-30%. In general, Hα ring galaxies take a large proportion of GV galaxies.

of 84) have the second peak detection. We denote the radial position of the first trough and the second peak as "gap radius" ($R_{\rm trough}$) and "ring radius" ($R_{\rm peak}$), respectively. To derive the measurement uncertainties of gap radius and ring radius, we cut the polar transformed flux distribution into three pieces, with each counts for 120 degrees in polar angle θ. Then we stack the Hα flux profiles within each piece and detect troughs and peaks for each stacked profile. After 100 times iteration, the standard variance of $R_{\rm trough}$ and $R_{\rm peak}$ are calculated and denoted as $\sigma_{\rm trough}$ and $\sigma_{\rm peak}$.

To investigate the relation between Hα ring radii and bar lengths, we use the bar length measurements $l_{\rm bar}$ in Galaxy Zoo 2 (GZ2) catalog. GZ2 measures detailed morphological features, including galactic bars, spiral arm, bulges, relative ellipticities and many others (Willett et al. 2013). We matched Hα ring galaxy sample with GZ2 bar length catalog (Hoyle et al. 2011) and obtain bar lengths data and their uncertainties for 19 galaxies (out of 84, in which 31 galaxies are barred according to Galaxy Zoo). Although this number is small, these 19 galaxies all have strong bars. Lower panels of Figure 4 show correlations between bar lengths and Hα ring radii. Figures 4(a) and 4(c) show that bar length $l_{\rm bar}$ is proportional to both gap radius $R_{\rm trough}$ and ring radius $R_{\rm peak}$. To eliminate the effect of PSF and galaxy's intrinsic size on bar length and Hα ring radius, we plot bar lengths and Hα ring radii in units of effective radii R_e in Figures 4(b) and 4(d). Clear linear correlations between $l_{\rm bar}/R_e$ and $R_{\rm peak}/R_e$, $R_{\rm trough}/R_e$ still exist.

The slopes of lines also reveal physical correlation between Hα ring and bar. We fit the straight lines in the lower panels of Figure 4 using MCMC algorithm with a one degree of freedom Student-t distribution as the prior distribution for the slope k and a top-hat distribution from -5 kpc to 5 kpc as the prior distribution for the intercept b. The uncertainties of slopes and intercepts shows 1σ confidence interval. The red lines show the best-fit results, and the blue dash-dotted lines have unity slope and zero intercept. The slopes of $l_{\rm bar}$–$R_{\rm peak}$ plot and $l_{\rm bar}/R_e$–$R_{\rm peak}/R_e$ are approximately unity, indicating that the bar is just stuck in the Hα ring. The relatively small scattering in intercept add credibility to this conclusion. Knowing that optical resonance ring usually coexists with bar and shares the same size, we suspect that Hα ring might be highly correlated to optical resonance ring. Supported by the above evidences, strong correlation among Hα ring, bar and optical ring exists. We will show more evidence from the perspective of bar fraction in Sections 4.1 and 5.

4. BAR, BULGE AND AGN

4.1. *Bar Fractions*

Section 3 already provides some evidence of the correlation between Hα rings and bars. In this section we calculate the fraction of barred galaxies in disk galaxies to further confirm this correlation and argue the importance of bar in the inside-out quenching process. Hereinafter we call this fraction as *bar fraction*. We use morphological classification results from the Galaxy Zoo Projects instead of our visual inspections to eliminate the subjective bias of visual inspection. Galaxy Zoo 1 (GZ1, Lintott et al. 2011) provides morphological classification for nearly one million galaxies in SDSS. Galaxies are classified into elliptical galaxy, spiral galaxy or uncertain morphology. We matched both total sample and Hα ring galaxy sample with GZ1 catalog to obtain morphological classification. 70 galaxies in Hα ring galaxy sample (out of 84) are matched in GZ1 catalog, while 2257 galaxies in total sample (out of 2704) are matched in GZ1 catalog. The numbers of disk galaxies, elliptical galaxies and uncertain galaxies in Hα ring galaxy sample are 44, 3 and 23. Disk galaxies, elliptical galaxies and uncertain galaxies account for 34.7%, 21.2% and 44.1% in 2257 Pipe3D galaxies, respectively.

As we mentioned in Section 3, Galaxy Zoo 2 (GZ2) contains classification of galaxy morphology in more details. Following the instructions from Willett et al. (2013), we diagnose barred galaxy with the following criteria: $p_{\rm features/disk} \geqslant 0.430$, $p_{\rm not-edge-on} \geqslant 0.715$, $p_{bar} \geqslant 0.4$ and $n_{\rm votes} \geqslant 10$. These thresholds give us 31 barred galaxies (out of 70, accounts for 44%) in Hα ring galaxy sample with GZ1 classification, and 259 barred galaxies (out of 2257, accounts for 11%) in total sample with GZ1 classification. As a comparison, there are 44 barred galaxies (out of 84, accounts for 52%) in Hα ring galaxy sample from visual inspection. We remind
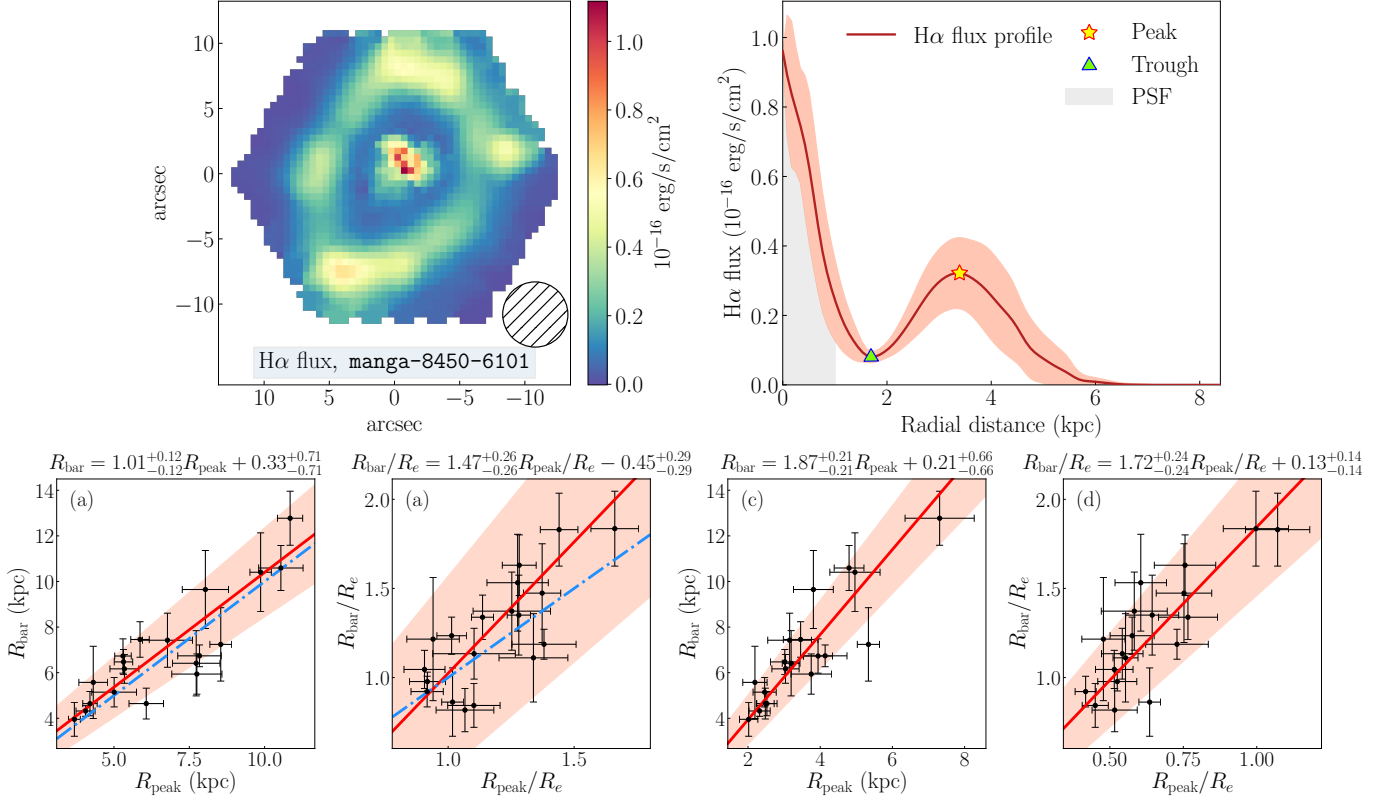
Figure 4. *Upper Panels:* The two-dimensional Hα flux image of galaxy `manga-8450-6101` is shown in the left panel. The corresponding Hα flux profile is also shown on right. A prominent Hα ring can be seen in the hexagonal FoV. We denote the radial position of the first trough as "gap radius" $R_{\rm trough}$, and the second peak as "ring radius" $R_{\rm peak}$. The corresponding physical size of point spread function (PSF) is denoted by the shaded circle in the left panel and gray area in the right panel, respectively. *Lower Panels:* We match Hα ring galaxy sample with Galaxy Zoo 2 catalog and obtain bar lengths data for 19 galaxies (out of 84). Panels (a) and (c) illustrate that bar length $l_{\rm bar}$ is proportional to both gap radius $R_{\rm trough}$ and ring radius $R_{\rm peak}$. Red lines are best linear fits while blue lines have unity slope and zero intercept. The shaded area indicates 1σ uncertainty. To eliminate any effect of PSF and galaxy's intrinsic size on the correlation between Hα ring and bar, we plot their relation again in units of effective radii R_e in Panels (b) and (d). These figures imply that Hα ring is strongly correlated to bar and optical ring.

our readers that in the calculation of bar fractions for both samples, we only use GZ2 classification of barred galaxies and GZ1 classification of disk galaxies to avoid subjective bias of visual inspection.

Based on the mass distribution of both Hα ring galaxy sample and total sample, we divide them into three stellar mass bins: $\log M_*/M_\odot = [10.0, 10.5]$, $[10.5, 11.0]$ and $[11.0, 11.5]$. Figure 5 shows the moving average of bar fraction as a function of specific Star Formation Rate (sSFR) for each mass bin, with 0.5 dex sSFR bin width and 0.05 dex moving step. In each mass bin and sSFR bin, the number of disk galaxies is the denominator of bar fraction, while the numerator is the number of barred galaxies. To ensure a higher statistical fidelity, we also neglect the data point if there are less than 3 disk galaxies ($n_{\rm disk} \leqslant 2$) in the corresponding mass bin and sSFR bin. Hence in Hα ring galaxy sample, bar fractions in mass bin $\log M_*/M_\odot = [10.0, 10.5]$ are not shown. The uncertainty of bar fraction is calculated by binomial standard deviation $\sigma_{p_{\rm bar}} = \sqrt{p_{\rm bar}(1 - p_{\rm bar})/n_{\rm disk}}$.

The bar fraction of Hα ring sample in $11.0 < \log M_*/M_\odot < 11.5$ (red line in Figure 5a) first rises rapidly when $\log$ sSFR < -10.5 yr^{-1}, and then remains almost constant when $\log$ sSFR > -10.5 yr^{-1}. Bar fractions in other mass bins almost remain constants, especially for total sample, but bar fraction of total sample in $11.0 < \log M_*/M_\odot < 11.5$ drops with sSFR increasing. To give more intuitive comparisons, we also plot the bar fractions in each mass bin (regardless of sSFR) for both samples, which are shown as pentagons for Hα ring galaxy sample and squares for total sample. The average bar fraction of Hα ring galaxy sample is around 0.5, whereas the average bar fraction of total sample is around 0.3. In each mass bin, the bar fractions of Hα ring galaxy sample is also higher than the corresponding bar fractions of total sample for about 20%. This implies that bar has a strong correlation with Hα ring, which is consistent with the result of Section 3. We will discuss the role of bar in the inside-out quenching in Section 5.
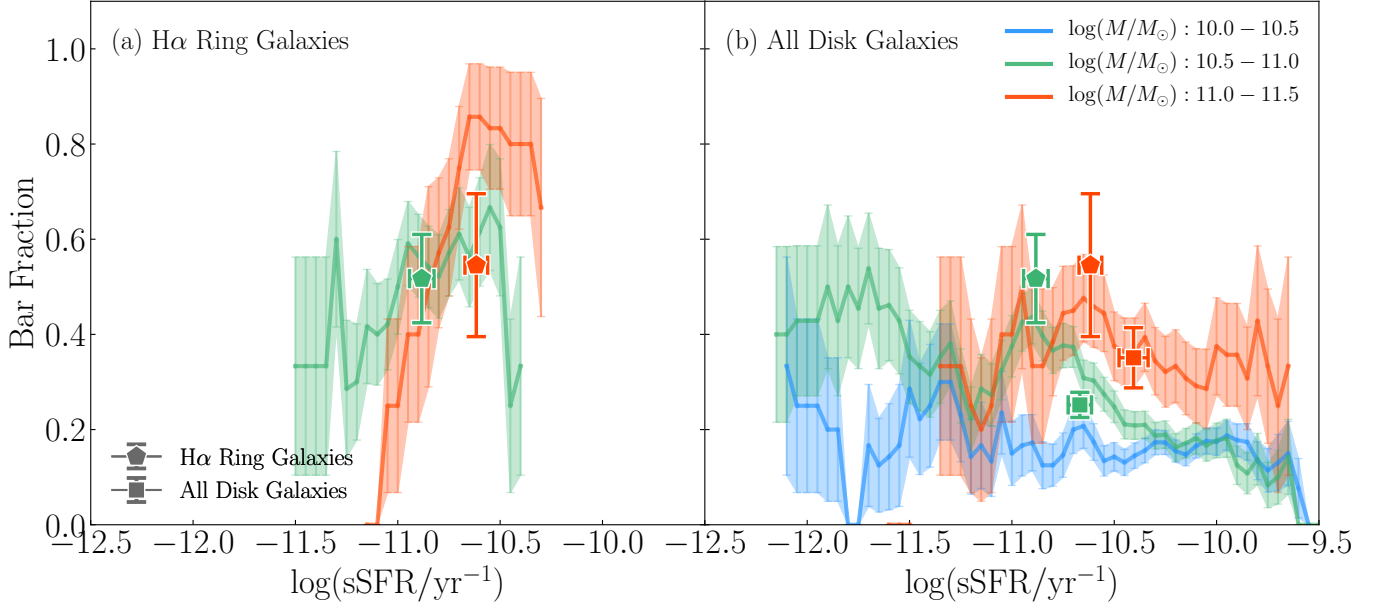
Figure 5. Bar fractions of Hα ring galaxy sample and total sample. Bar fractions are calculated with respect to disk galaxies. Red, green and blue lines represent three stellar mass bins: $\log M_*/M_\odot = [10.0, 10.5]$, $[10.5, 11.0]$ and $[11.0, 11.5]$, respectively. The average bar fraction of Hα ring galaxy sample is about 50%, higher than that of total sample (about 30%). No matter in which mass bin or in total, bar fraction of Hα ring galaxy sample are higher than that of total sample.

4.2. AGN Fractions

In our Hα ring sample, given a high bar fraction, we may also expect LLAGN activities and thus inside-out quench these galaxies by the AGN feedback. To get a more comprehensive understanding of these Hα ring galaxies, we first diagnose excitation types of galaxy nuclei using BPT diagrams (Baldwin et al. 1981; Veilleux & Osterbrock 1987), and then calculate the AGN fractions to explore the relation between AGN and the quenching of Hα ring galaxies. We remind our readers that AGN here includes both Seyfert and LINER galaxy.

In the past, people classified galaxies based on BPT diagrams using the spectra of galaxy nuclei obtained by single fibre. The corresponding physical sizes of a single fiber could change dramatically with redshift. Now with MaNGA IFU data, we can spacially map the excitation properties for galaxies, and diagnose excitation type of galaxy nuclei within a fixed physical aperture (Fu et al. 2018). Over the redshift range $0.01 < z < 0.15$, the angular scale increases from 0.20 kpc/arcsec to 2.58 kpc/arcsec. We choose an appropriate physical aperture diameter to be 2.6 kpc, which corresponds to half of the fiber diameter (1 arcsec) at highest redshift and also allows the smallest IFU FoV (12 arcsec diameter) containing this physical size for nearest galaxies. In the following, the fluxes of emission lines are all measured within this 2.6 kpc nuclear aperture. We also assign the nuclear EW[Hα] to be the mass weighted average for EW[Hα] of each spaxel inside the 2.6 kpc nuclear aperture.

Cid Fernandes et al. (2011) showed that equivalent width of Hα emission line (EW[Hα]) indicates the dominance of pAGB stars robustly: The emission lines caused by pAGB stars typically has lower equivalent widths. To separate "retired galaxies" whose excitation properties are dominated by hot evolved stars, we adopt an empirical demarcation EW[Hα]= 3Å. We classify galaxies with EW[Hα]< 3Å as RG and then only classify the excitation types of galaxies which are not RGs using BPT diagrams. The cut of Hα equivalent width at 3Å also removed those galaxies with insufficient signal-to-noise ratio (S/N) for any of the four emission lines used in BPT diagrams. Figure 6 presents BPT diagrams for both sample. Pentagrams shows galaxies in Hα ring sample, whereas galaxies in total sample are shown as dots in background. They are all with color-coded by nuclear excitation types. Demarcation lines in BPT diagrams are adopted from Kauffmann et al. (2003) and Kewley et al. (2006). We find 8 star-forming galaxies (SFs), 9 LINERs and 1 Seyfert galaxy in Hα ring galaxy sample, while the remaining 66 galaxies are all RGs. Combining the visual inspection results, there are 8 barred galaxies which have AGNs, 36 bared galaxies which do not have AGNs, 39 unbarred galaxies which do not have an AGN, and only 1 unbarred galaxy which has an AGN. In total sample, SFs, LINERs, Seyferts and retired galaxies account for 47.3%, 6.0%, 1.3% and 45.3% respectively. It's worth noticing that the proportion of RGs is much higher in Hα ring galaxy sample (80%) than in total sample (45%). If we mark these RGs on BPT diagrams, they are mainly located in LINER region.
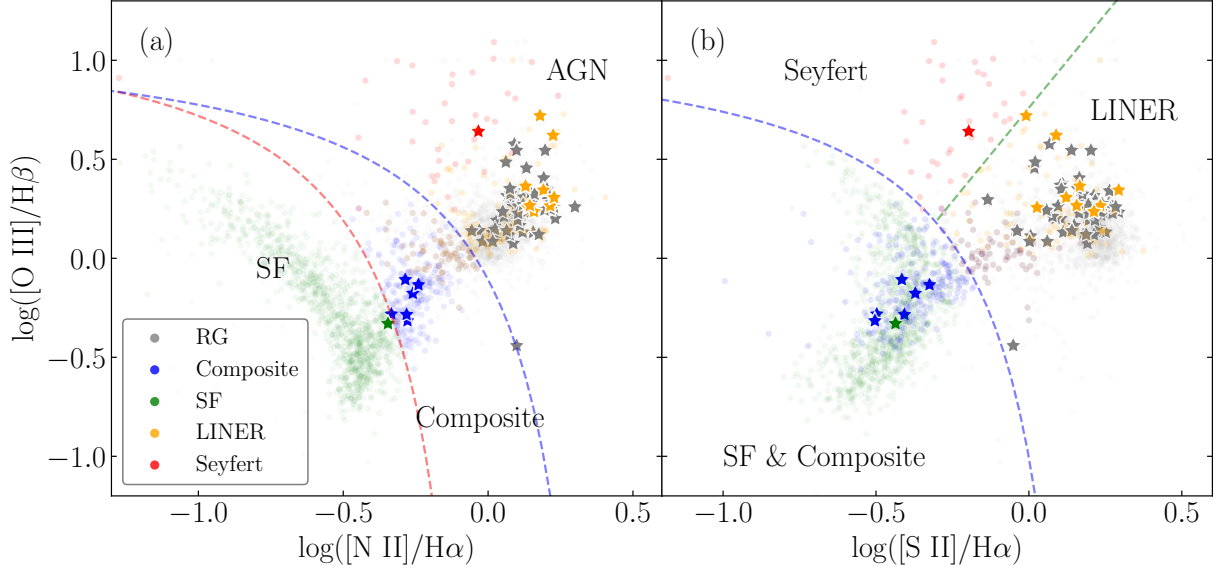
Figure 6. BPT diagrams for Hα ring galaxy sample (pentagrams) and total sample (dots). We measure the nuclear emission line fluxes within 2.6 kpc aperture and calculated nuclear EW[Hα] as mass-weighted value of each spaxel. After assigning galaxies with EW[Hα]< 3Ås as RGs, we classify the excitation types of the remaining galaxies using BPT diagrams. We find 8 SFs, 9 LINERs and 1 Seyfert galaxy in Hα ring galaxy sample, while the remaining 66 galaxies are all RGs. In total sample, SFs, LINERs, Seyferts and RGs account for 47.3%, 6.0%, 1.3% and 45.3%, respectively.
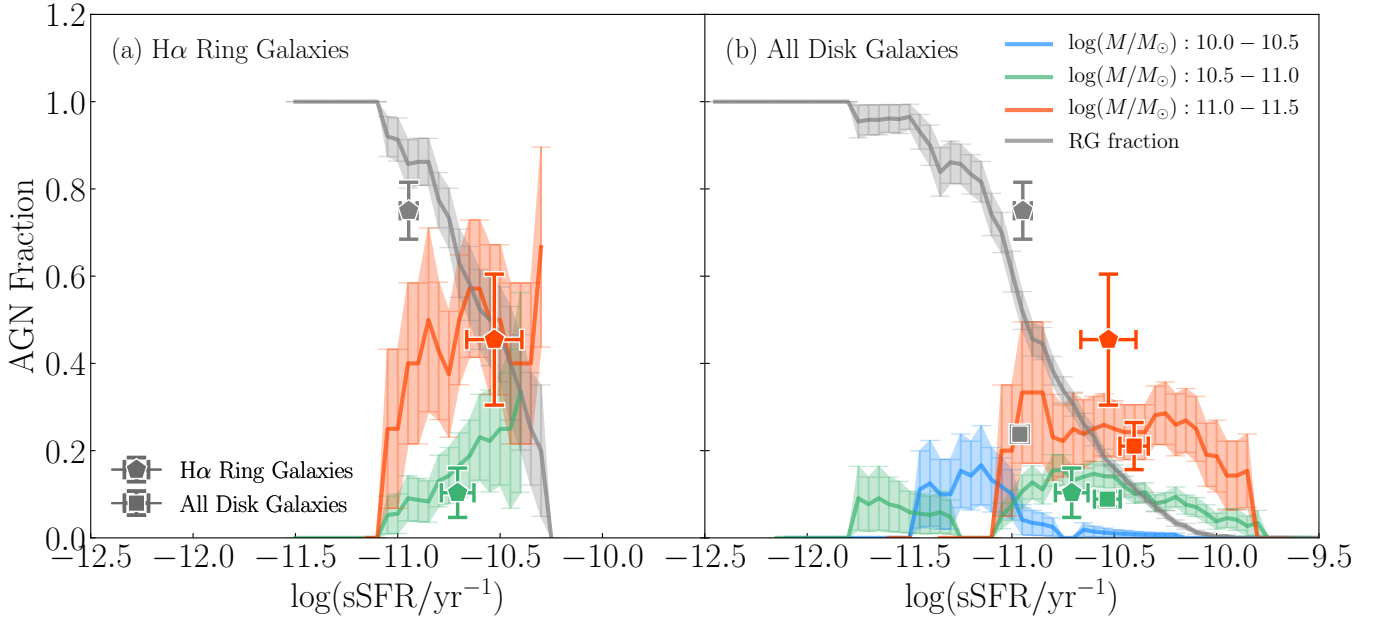
Figure 7. AGN fractions of Hα ring galaxy sample and total sample. AGN fractions are calculated with respect to disk galaxies based on AGN diagnosis in Figure 6. Lines are color-coded by stellar mass bins, and gray lines present retired galaxy (RG) fractions. We remind our readers that AGNs contain Seyfert galaxies and LINERs. AGN fraction in Hα ring sample is higher than that in total sample overall, but the difference is not very significant compared with bar fractions in Figure 5.

Following the traditional definition, we consider AGNs to contain Seyfert galaxies and LINERs. With the diagnosis of nuclear excitation types, we calculate the fraction of AGN galaxies in disk galaxies for both samples, and we refer to this fraction as *AGN fraction* hereinafter. Figure 7 presents the moving average of AGN fraction as a function of sSFR for each mass bin in both samples. The details here are the same as calculating bar fractions in Section 4.1. The AGN fractions in each mass bin (regardless of sSFR) are also shown in pentagons for Hα ring galaxy sample and squares for total sample. Given that most AGNs here are LINERs, the AGN fractions are actually dominated by LINER fractions.

In mass bin $10.5 < \log M_*/M_\odot < 11.0$ (green lines), AGN fraction of Hα ring sample is slightly higher than that of total sample, especially at higher sSFR end. AGN fraction of Hα ring galaxies in $11.0 < \log M_*/M_\odot < 11.5$ (red line) is much higher than that of total galaxies in the same mass bin, with average value ~ 0.45 and ~ 0.2 respectively. Furthermore, the AGN fractions of Hα ring galaxy sample are rising along sSFR. But for total sample, AGN fractions drop or remain constant with sSFR increasing. On average, AGN fraction of disks in Hα ring galaxy sample is higher than that of total sample, but the difference is not as significant as in bar fraction.

Gray lines in Figure 7 are the retired galaxy (RG) fractions. It's notable that RG fraction declines slower in Hα ring galaxy sample than in total sample, and is higher than that of total sample, especially in high sSFR region. The overall RG fraction in Hα ring sample (~ 0.75) is higher than that of total sample (~ 0.25) for nearly three times. Combining the LINER fraction in the classifications and moving average of AGN fraction, Figures 6 and 7 imply that AGN (Seyfert/LINER) is also related the inside-out quenching of Hα ring galaxies. High RG fraction and LINER fraction in Hα ring sample can be natural consequences of inside-out quenching. More detailed discussions on LINER and inside-out quenching are in Section 5.

4.3. *Morphological Quenching and Bulge*

"Morphological quenching" (or "gravitational quenching") provides a probably explanation for the suppress of star formation in massive disk galaxies (Martig et al. 2009). Prominent bulges in the center of galaxies could increase the Toomre Q parameter (Toomre 1964), so that the disk will be stable against collapse and form stars. Thus the absence of star formation in the center of galaxy can be naturally caused by the growth of bulge. This quenching mode is correlated to the presence of bulge (and also pseudo-bulge) and bulge-to-total ratio.

To investigate the importance of morphological quenching in the inside-out quenching of our Hα galaxy sample, we match disks in our samples with the bulge-disk decomposition results in Mendel et al. (2014)
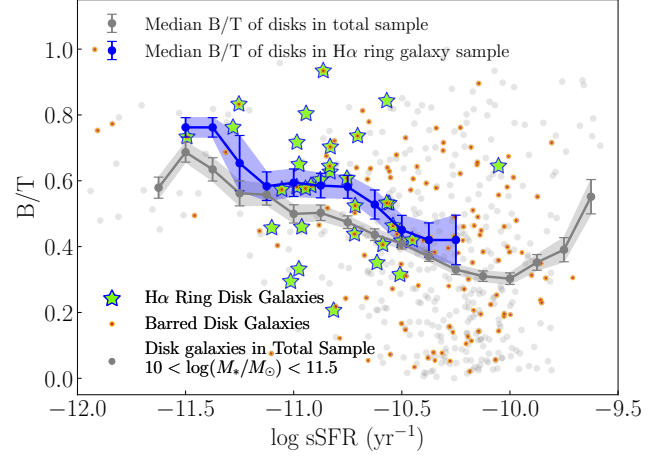

Figure 8. Mass weighted bulge-to-total ratio (B/T) decreases with increasing sSFR. Gray dots are disk galaxies in total sample with $10.0 < \log(M/M_\odot) < 11.5$, and green stars are galaxies in Hα ring sample. Barred disk galaxies are highlighted by orange dots. Gray and blue lines show how the median of B/T ratios vary with sSFR in total sample and Hα ring sample, respectively. They have the same decreasing trend, but B/T ratio of Hα ring sample is higher than that of total sample. This implies that the joint actions of bar, AGN and bulge could probably quench the galaxy by the inside-out mode efficiently.

and calculate mass-weighted bulge-to-total (B/T) ratio (mass is estimated in dust-free models). Considering the distribution of stellar mass in Hα ring sample, we only compare galaxies within $10.0 < \log(M/M_\odot) < 11.5$ to eliminate the interference of low mass/high mass spirals in total sample. Thirty-four disk galaxies in Hα ring galaxy sample get matched in B/T ratio catalog. We calculated the moving median of mass weighted B/T ratio for disks in Hα ring galaxy sample (green stars in Figure 8) and disks in total sample (gray dots in Figure 8) with sSFR bin = 0.5 dex and step size 0.1 dex. Orange dots are barred disk galaxies in total sample. Figure 8 shows that B/T ratios of disk galaxies decrease with sSFR increasing in both samples. Figure 8 also presents that median B/T ratio of Hα ring galaxy sample is slightly higher than that of total sample for about 0.1. This implies that morphological quenching might not be the dominant quenching channel of these inside-out quenching Hα ring galaxies. However, the larger B/T ratio, high bar fraction and high AGN fraction do suggest that the joint action of bar, AGN and bulge quench galaxies efficiently.

5. DISCUSSION

5.1. *Inside-out quenching, Hα ring and Optical ring*

Inside-out quenching was suggested by various observations of galaxy SFR and mass profiles at different stage in their lifetime (Tacchella et al. 2015, 2018). In a theoretical view of inside-out quenching, the disk in-

stability first induce gas inflow and trigger starburst in galactic center, then the inflow gas could fuel central AGN and cause AGN feedback to cease the star formation in galactic center. Bar and bulge-driven process can also stabilize the gas in galactic center and prevent further star formation. After been quenched at center, the outskirts still remain high star formation rate. The inside-out quenching naturally make a ring-like star forming structure outside the quenched region, which is just the Hα ring-like structure. Our finding here is consistent with stacking analysis in Guo et al. (2019).

From visual inspection, we noticed that optical rings have the same size as Hα ring for some galaxies in Hα ring sample. In observations, optical ring structures are divided into inner ring and outer ring. Inner rings basically encircled the end of the bar, while outer rings are typically 1.2 times larger than the bar length (Kormendy 2013). Here we do not take the nuclear ring ($r < 1$ kpc) into account because of the limitation of spacial resolution. Both inner ring and outer ring typically contains HI gas and star formation. Most galaxies with optical ring also have bars. Bar can also contribute to the formation of optical rings. The result of Section 3 suggests strong correlation between bar length and Hα ring size. Since we didn't select the Hα ring sample from optical images, Hα ring can be different from optical ring. But this correlation implies the coincidence between Hα ring and optical inner ring. Higher bar fraction in Hα ring galaxy sample also indicates a strong correlation between rings and bar.

Ring structures are commonly found in the galaxy simulations. *Illustris* team studied the morphology of nearby galaxies at $z = 0$ and found a sizable proportion of galaxies within $10.5 < \log M_*/M_\odot < 11$ have a distinct ring or a C-shape morphology (Snyder et al. 2015), which is contradict with observations. However, in the Illustris TNG (Nelson et al. 2018; Springel et al. 2018), the ring galaxies are not as plentiful as before. The equation of state of ISM pressurization, stellar feedback models and AGN feedback models can affect how gas piles up in galaxy formation, thereby change the morphology (Pillepich et al. 2018; Weinberger et al. 2017). In further study, we will use simulations to investigate the formation of rings and the inside-out quenching process.

5.2. Environment

P-type and O-type optical ring galaxies have different formation mechanisms. The collision-originated ring galaxies (P-type) are more likely to live in denser environment than the resonance ring galaxies (O-type), since it's much more probable to have collisions and drop-through interactions in compact groups and clusters (Elagali et al. 2018). Many collision-originated ring galaxies are indeed located within galaxy groups which have at least one companion galaxy (Romano et al. 2008).

We cross-matched both Hα ring galaxy sample and total sample with the density field catalog calculated by Peng et al. (2010), and got 56 Hα ring galaxies with density filed data. Here the over-density is denoted as $\delta = (\rho - \rho_m)/\rho_m$, where ρ_m is the volume mean density. The upper panel of Figure 9 shows the normalized distribution of galaxies along $\log(1 + \delta)$. Galaxies in both samples are mainly located in $-0.5 < \log(1 + \delta) < 1.0$, and no significant difference is found between the two samples. The lower panel shows the normalized distribution of barred disk galaxies in both samples. Total numbers of barred disk galaxies in both samples are 121 (total sample) and 20 (Hα ring sample). Over 90% barred disk galaxies in Hα ring sample live in the environment with $\log(1 + \delta) > 0.5$, which is 17% higher than that in total sample. Although Skibba et al. (2012) found that barred and bulge dominated galaxies tend to be found in denser environments than unbarred counterparts, we think the environmental difference in our samples is probably caused by the small sample size.

In the selection of Hα ring galaxy sample, we didn't distinguish between P-type Hα ring and O-type Hα ring. We only focus on the ring-like structure and the gap between the central region and Hα ring in the tri-color emission-line image. Figure 9 doesn't show conspicuous environmental difference between the two sample. Since we have found high bar fraction and good relation between bar and Hα ring, the majority of Hα ring galaxies are probably not collision-originated. Considering that galaxies in Hα ring sample have are relatively massive, so that their evolution are less affected by environments. Hence the irrelevance of environment found in Figure 9 is reasonable.

5.3. Bar and Bulge

The effects of bar on the secular evolution of disk galaxies are studied in various simulations. Bar drives gas toward galactic center, triggers star formation, lowers the gas content and probably feeds central AGN (Kormendy & Kennicutt 2004; Lin et al. 2017). Bar quenching is suggested by many authors from both observation and simulation (Gavazzi et al. 2015; Kruk et al. 2018). In observation, barred disk galaxies are significantly redder compared to unbarred galaxies, implying that bar-driven activities may have non-negligible influence in the evolution of disk galaxies. In the cosmological "zoom-in" simulation of Milky Way-type galaxy, Spinoso et al. (2017) find that bar is very efficient in transforming gas within bar co-rotation radius into galactic center at the onset of bar formation. When bar is well developed, the inner parts of galaxy has already been depleted, quenched and become a 'dead zone', which is consistent with the cessation of star formation within Hα ring. Besides, Robichaud et al. (2017) compares star formation maps of disk galaxies with and without bars. The existence of bar could lead to the appearance of star formation ring at large radii, which could explain the high
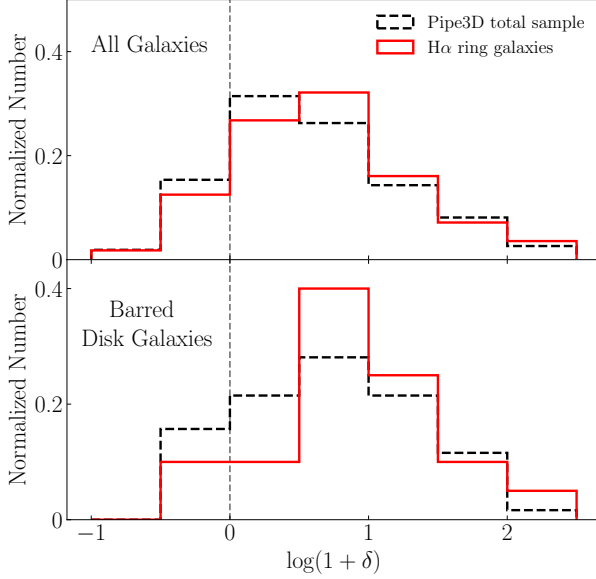
Figure 9. Distributions of environment over-density for both Hα ring galaxy sample and total sample. The lower panel only shows distribution of barred disk galaxies. We do not see conspicuous environmental difference between two sample, which implies that the majority of Hα rings are not collision-originated.

bar fraction in Hα ring sample naturally. We also noted that the distribution of barred galaxies on stellar mass M_*–SFR diagram (Figure 2) is nearly uniform, indicating the availability of bar quenching in different mass range.

Many works have found that the secular evolution of barred disk galaxies will lead to the appearance of pseudo-bulge (Kormendy & Kennicutt 2004; Kruk et al. 2018 and references there in). Classical bulge (Sersic index $n_{\rm bulge} > 2$) can be formed by major and minor mergers, while pseudo-bulge (Sersic index $n_{\rm bulge} < 2$) is formed by secular evolution of disk galaxy (Fisher & Drory 2008). The decomposition analysis points out that most bulges in barred galaxies are indeed pseudo-bulge (Kruk et al. 2018), suggesting that bar adds mass into the bulge during the secular evolution. Within the morphological quenching scenario, given the high bar fraction in Hα ring galaxies, we expect high B/T ratio correspondingly. However, there are some evidence against the trend that bar induce the growth of pseudo-bulge. Laurikainen et al. (2013) find lower B/T ratio in strongly barred galaxies compared to unbarred galaxies, while this trend also holds for less massive galaxies in Kruk et al. (2018). In Section 4.3, we check the reliance of B/T ratio on Hα ring and find that B/T ratio of Hα ring sample is indeed higher, which is consistent with our speculation. But the credibility of this conclusion is still limited by the small size of Hα ring galaxy sample and large scattering of B/T ratios.

5.4. *Active Galactic Nuclei (AGN)*

Active galactic nuclei (AGN) has long been suspected to quench galaxies, and its role has been debated for a long time (Ref. here). Many works have studied AGN feedback from both observation side (Ref. here) and simulation side (Ref. here). AGN feedback is recently added into the recipe of simulations and has already achieved agreement with observations. The basic scenario is that AGN activities blow out and heat the cold gas, preventing further star formation. Besides, bar induced gas inflow could fuel the central AGN and trigger feedback to suppress star formation in the central region. AGN photoionization model has been success in explaining the exsitence of low-ionization nuclear emission-line region (LINER) (Ho et al. 1997; Ho 2008). Given the ubiquity of LINER and low-luminosity AGN (LLAGN) in nearby galaxies, LLAGN feedback can be the main channel of AGN feedback.

Despite the success of AGN model, recent studies have pointed out that many LINERs are not consistent with the hypothesis that LINER is only powered by LLAGN. Old evolved stars such as post-asynmptotic giant branch (pAGB) stars are hot enough to ionized the nearby gas and produce LINER-like emission line ratios (Cid Fernandes et al. 2011; Belfiore et al. 2016, 2018). The light of hot old stars was overwhelmed by the light of young stars in star forming regions. After star forming regions have been quenched, the dominated hot old stars could produce LINER-like emission properties. Observation has found that LINER regions are quite extended, typically kpc scale. The extended LINER region can hardly caused by LLAGN, whose influence is usually limited within several hundred parsec.

The high AGN and LIER fraction found in Hα ring galaxy sample agrees with the LIER sequence in Hsieh et al. (2017) and central low-ionization emission-line regions (cLIERs) in Belfiore et al. (2016). The extended (kpc scale) LIER regions are more likely to be caused by hot evolved stars rather than low luminosity AGNs. We further inspect our Hα ring sample using the BPT map proposed in Belfiore et al. (2016), see Figure 10 as an example. In Figure 10, we assign spaxels where EW[Hα]< 1Å to be line-less region. Since our IFU map is not Voronoi binned (Cappellari & Copin 2003), the cut on EW excludes low S/N spaxels effectively. The shaded circle in right-bottom corner represent PSF scale. In Hα ring sample, all LINERs (9 in total) are cLIERs, and most (85%) RGs are also cLIERs. We notice that in Figure B1 of Belfiore et al. (2017), many galaxies in cLIER sample could be diagnosed to have Hα ring. We further calculate the cLIER area and derive a equivalent radius of cLIER region for all RG galaxies and LINERs (which are diagnosed in Figure 6) in our Hα ring sample.

The cLIER area A is calculated by counting LIER spaxels within a given aperture R. We first define r_{60}
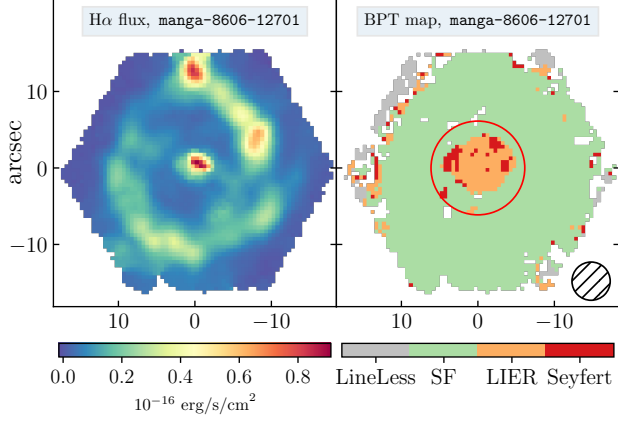
Figure 10. Hα flux image and BPT map of Hα ring galaxy `manga-8606-12701`. This galaxy is diagnosed as cLIER. We assign spaxels where EW[Hα]< 1Å to be line-less region (gray in this figure). The shaded circle in right-bottom corner represents PSF scale.
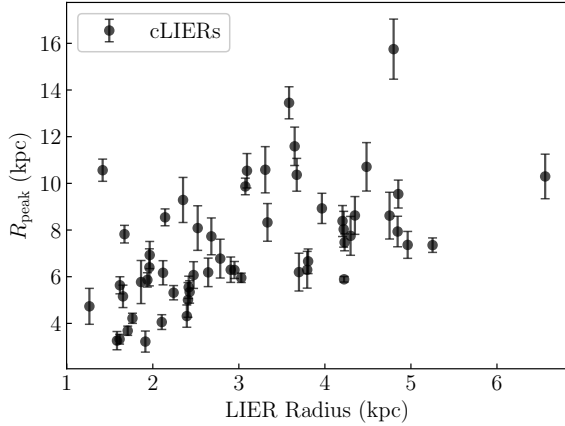

Figure 11. The radius of cLIER region is logarithm proportional to Hα ring radius. We first calculate cLIER area by counting LIER spaxels within a given aperture, and then derive cLIER radius by $r = \sqrt{A/\pi}$. We visually checked and confirmed the rationality of the calculation. The proportional relation supports that cLIER region is mainly caused by pAGB stars.

to be that within which the LIER spaxels account for 60% of total LIER spaxels. Then the aperture R is defined as the minimum between r_{60} and half of FoV. The equivalent radius of cLIER region is simply defined as $r = \sqrt{A/\pi ba}$, where ba is the minor-to-major axis ratio. We checked the rationality of the calculation of cLIER area by visual inspection. Figure 11 shows logarithm linear relation between cLIER radius and Hα ring radius. If cLIER is LLAGN activity only, its radius cannot be so dependent on Hα ring size (and galaxy size). This result supports that cLIER is mainly excited by pAGB stars instead of LLAGN.

However, in nearby LINER host galaxies, most of them (57 in 66) have X-ray active cores, implying that they are genuine AGN (She et al. 2017). Green valley galaxies in Guo et al. (2019) and our Hα ring galaxies are quite alike. Guo et al. (2019) argue that the point-source-like central peak of Hα radial profile cannot be simply explained by hot evolved stars and prefer the existence of pure AGNs. Simulations also find the existence of bar could enhance AGN feedback effect (Robichaud et al. 2017). We already talked about the close relation between bar and bulge in Section 5.3. The tight relation between galaxy central black hole mass and its bulge mass also exists (Wandel 1999, 2002; Merritt & Ferrarese 2001). In Section 4.2, we calculated AGN (Seyfert and LINER) fractions and found that Hα ring galaxies has relatively high LINER and RG fraction. The results of high bar fraction, high B/T ratio and high AGN fraction are consistent with each other. The bar-induced activities fuel the central AGN and contribute to the growth of bulge, and the actions of AGN feedback, bar-induced gas depletion and morphological quenching jointly lead to the inside-out quenching of these Hα ring galaxies.

Spinoso et al. (2017) suggest that the absence of clear correlation between bar and AGN activity could be related to the fast consumption of gas when bar just starts to form, i.e. the time delay between AGN activity and appearance of strong bar. When AGN is active at the onset of bar, the bar is small and irregular in shape, making it hard to be detected using imaging and photometry. When bar becomes stronger, central AGN has been turned off and star formation has been ceased within a ring structure. The 'dead' region is dominated by hot evolved stars and behaves like LIER region. High AGN/RG fraction, high bar fraction, high B/T ratio and tight relation between bar and Hα ring in our findings are quite consistent with this scenario. However, our findings still cannot really disentangle the effect of LLAGN from old evolved stars because of limitation of spacial resolution.

6. CONCLUSION

Based on MaNGA IFU spectroscopic data of 2704 nearby galaxies in data release MaNGA v2_1_2, we identified 84 galaxies with prominent Hα ring-like structures, with their stellar mass in the range of $9.5 < \log(M_*/M_\odot) < 11.5$. We measured the radii of Hα rings and compared with bar lengths. Bar fraction, AGN fraction and bulge-to-total ratio are also calculated for both sample. The roles of environment and various internal processes in the quenching of disk galaxies are also discussed. We summarize the main results of our work as follows:

1. Galaxies with Hα ring-like structures are in "inside-out" quenching processes and mostly located in the "green valley". These galaxies account for 20% - 30% in green valley galaxies.

2. The radii of Hα ring has strong linear relations with bar lengths. We excluded the possibility that PSF and intrinsic physical size of galaxies affect this relation. The bar fraction of Hα ring sample is higher than that of total sample for 20%-30% in each mass bin. The average bulge-to-total ratio of Hα sample is slightly higher for 5%-10% than that of total sample. These pieces of evidence imply that bar and bulge play very important roles in quenching disk galaxies by inside-out mode.

3. LINERs account for a large proportion in both sample, but the LINER fraction is much higher in Hα ring galaxy sample. The AGN (Seyfert/LINER) fraction of Hα ring galaxy sample is also higher than that of total sample for about 10%. The AGN fraction is especially higher in [11.0, 11.5] mass bin. This suggests that AGN feedback may play some roles in the inside-out quenching process of these galaxies. In the study of BPT maps, we found that 85% RGs and all LINERs in Hα ring galaxy sample are cLIERs. We also measured the radii of cLIERs and compared them with ring radii $R_{\rm peak}$. The proportionality supports that cLIER emission is mainly powered by hot evolved stars rather than pure AGN.

4. Considering high bar fraction, AGN fraction, B/T ratio in Hα ring galaxy sample and tight correlation between bar and Hα ring, we suggest that the inside-out quenching process of massive disk galaxies is mainly caused by the joint effects of bar, AGN and bulge. Besides, environmental factor does not affect the quenching of Hα ring galaxies obviously.

REFERENCES

Abazajian, K. N., Adelman-McCarthy, J. K., Agüeros, M. A., et al. 2009, ApJS, 182, 543

Astropy Collaboration, Robitaille, T. P., Tollerud, E. J., et al. 2013, A&A, 558, A33

Baldwin, J. A., Phillips, M. M., & Terlevich, R. 1981, PASP, 93, 5

Belfiore, F., Maiolino, R., Maraston, C., et al. 2016, MNRAS, 461, 3111

—. 2017, MNRAS, 466, 2570

Belfiore, F., Maiolino, R., Bundy, K., et al. 2018, MNRAS, 477, 3014

Brinchmann, J., Charlot, S., White, S. D. M., et al. 2004, MNRAS, 351, 1151

Bundy, K., Bershady, M. A., Law, D. R., et al. 2015, ApJ, 798, 7

Buta, R. J. 2017, Monthly Notices of the Royal Astronomical Society, 471, 4027

Cappellari, M., & Copin, Y. 2003, MNRAS, 342, 345

Cid Fernandes, R., Stasińska, G., Mateus, A., & Vale Asari, N. 2011, MNRAS, 413, 1687

Croom, S. M., Lawrence, J. S., Bland-Hawthorn, J., et al. 2012, MNRAS, 421, 872

Dekel, A., & Burkert, A. 2014, MNRAS, 438, 1870

Drory, N., MacDonald, N., Bershady, M. A., et al. 2015, AJ, 149, 77

Elagali, A., Lagos, C. D. P., Wong, O. I., et al. 2018, ArXiv e-prints, arXiv:1807.08251

Falcón-Barroso, J., Sánchez-Blázquez, P., Vazdekis, A., et al. 2011, A&A, 532, A95

Few, J. M. A., & Madore, B. F. 1986, Monthly Notices of the Royal Astronomical Society, 222, 673

Fisher, D. B., & Drory, N. 2008, AJ, 136, 773

Foreman-Mackey, D., Hogg, D. W., Lang, D., & Goodman, J. 2013, Publications of the Astronomical Society of the Pacific, 125, 306

Fu, H., Steffen, J. L., Gross, A. C., et al. 2018, ApJ, 856, 93

Gallart, C., Stetson, P. B., Meschin, I. P., Pont, F., & Hardy, E. 2008, ApJ, 682, L89

Gavazzi, G., Consolandi, G., Dotti, M., et al. 2015, A&A, 580, A116

Gunn, J. E., Siegmund, W. A., Mannery, E. J., et al. 2006, AJ, 131, 2332

Guo, K., Peng, Y., Shao, L., et al. 2019, ApJ, 870, 19

Ho, L. C. 2008, ARA&A, 46, 475

Ho, L. C., Filippenko, A. V., & Sargent, W. L. W. 1997, ApJ, 487, 568

Hoyle, B., Masters, K. L., Nichol, R. C., et al. 2011, MNRAS, 415, 3627

Hsieh, B. C., Lin, L., Lin, J. H., et al. 2017, ApJL, 851, L24

Hubble, E. P. 1926, ApJ, 64, doi:10.1086/143018

Hunter, J. D. 2007, Computing in Science Engineering, 9, 90

Jones, E., Oliphant, T., Peterson, P., et al. 2001–, SciPy: Open source scientific tools for Python

Kauffmann, G., Heckman, T. M., Tremonti, C., et al. 2003, MNRAS, 346, 1055

Kennicutt, Jr., R. C. 1998, ApJ, 498, 541

Kewley, L. J., Groves, B., Kauffmann, G., & Heckman, T. 2006, MNRAS, 372, 961

Kormendy, J. 2013, Secular Evolution in Disk Galaxies, ed. J. Falcón-Barroso & J. H. Knapen, 1

Kormendy, J., & Kennicutt, Jr., R. C. 2004, ARA&A, 42, 603

Kruk, S. J., Lintott, C. J., Bamford, S. P., et al. 2018, MNRAS, 473, 4731

Larson, R. B., Tinsley, B. M., & Caldwell, C. N. 1980, ApJ, 237, 692

Laurikainen, E., Salo, H., Athanassoula, E., et al. 2013, MNRAS, 430, 3489

Law, D. R., Yan, R., Bershady, M. A., et al. 2015, AJ, 150, 19

Li, C., Wang, E., Lin, L., et al. 2015, ApJ, 804, 125

Lin, L., Li, C., He, Y., Xiao, T., & Wang, E. 2017, ApJ, 838, 105

Lintott, C., Schawinski, K., Bamford, S., et al. 2011, MNRAS, 410, 166

Martig, M., Bournaud, F., Teyssier, R., & Dekel, A. 2009, ApJ, 707, 250

Mendel, J. T., Simard, L., Palmer, M., Ellison, S. L., & Patton, D. R. 2014, ApJS, 210, 3

Merritt, D., & Ferrarese, L. 2001, 249, 335

Negri, L. H., & Vestri, C. 2017, lucashn/peakutils: v1.1.0, doi:10.5281/zenodo.887917

Nelson, D., Pillepich, A., Springel, V., et al. 2018, MNRAS, 475, 624

Pan, Z., Li, J., Lin, W., et al. 2015, ApJL, 804, L42

Peng, Y., Maiolino, R., & Cochrane, R. 2015, Nature, 521, 192

Peng, Y.-j., Lilly, S. J., Kovač, K., et al. 2010, ApJ, 721, 193

Pérez, E., Cid Fernandes, R., González Delgado, R. M., et al. 2013, ApJL, 764, L1

Pillepich, A., Springel, V., Nelson, D., et al. 2018, MNRAS, 473, 4077

Robichaud, F., Williamson, D., Martel, H., Kawata, D., & Ellison, S. L. 2017, MNRAS, 469, 3722

Romano, R., Mayya, Y. D., & Vorobyov, E. I. 2008, The Astronomical Journal, 136, 1259

Salpeter, E. E. 1955, ApJ, 121, 161

Sánchez, S. F. 2006, Astronomische Nachrichten, 327, 850

Sánchez, S. F., Kennicutt, R. C., Gil de Paz, A., et al. 2012, A&A, 538, A8

Sánchez, S. F., Pérez, E., Sánchez-Blázquez, P., et al. 2016, RMxAA, 52, 171

Sánchez, S. F., Avila-Reese, V., Hernandez-Toledo, H., et al. 2018, RMxAA, 54, 217

Sánchez-Blázquez, P., Forbes, D. A., Strader, J., Brodie, J., & Proctor, R. 2007, MNRAS, 377, 759

She, R., Ho, L. C., & Feng, H. 2017, ApJ, 835, 223

Skibba, R. A., Masters, K. L., Nichol, R. C., et al. 2012, MNRAS, 423, 1485

Smee, S. A., Gunn, J. E., Uomoto, A., et al. 2013, AJ, 146, 32

Snyder, G. F., Torrey, P., Lotz, J. M., et al. 2015, Monthly Notices of the Royal Astronomical Society, 454, 1886

Spinoso, D., Bonoli, S., Dotti, M., et al. 2017, MNRAS, 465, 3729

Springel, V., Pakmor, R., Pillepich, A., et al. 2018, MNRAS, 475, 676

Tacchella, S., Carollo, C. M., Renzini, A., et al. 2015, Science, 348, 314

Tacchella, S., Carollo, C. M., Schreiber, N. M. F., et al. 2018, The Astrophysical Journal, 859, 56

Toomre, A. 1964, ApJ, 139, 1217

van der Walt, S., Colbert, S. C., & Varoquaux, G. 2011, Computing in Science Engineering, 13, 22

Vazdekis, A., Sánchez-Blázquez, P., Falcón-Barroso, J., et al. 2010, MNRAS, 404, 1639

Veilleux, S., & Osterbrock, D. E. 1987, ApJS, 63, 295

Wake, D. A., Bundy, K., Diamond-Stanic, A. M., et al. 2017, AJ, 154, 86

Wandel, A. 1999, ApJL, 519, L39

—. 2002, ApJ, 565, 762

Wang, J., Kauffmann, G., Overzier, R., et al. 2011, MNRAS, 412, 1081

Weinberger, R., Springel, V., Hernquist, L., et al. 2017, MNRAS, 465, 3291

Willett, K. W., Lintott, C. J., Bamford, S. P., et al. 2013, MNRAS, 435, 2835